ACS NANO

www.acsnano.org

ARTICLE

Generation and Propagation of Flexoelectricity-Induced Solitons in Nematic Liquid Crystals

Xingzhou Tang, Noe Atzin, Ali Mozaffari, Soumik Das, Nicholas L. Abbott, and Juan J. de Pablo*

Cite This: *ACS Nano* 2024, 18, 10768–10775

Read Online

ACCESS | Metrics & More | Article Recommendations | Supporting Information

ABSTRACT: **Solitons in nematic liquid crystals facilitate the rapid transport and sensing in microfluidic systems. Little is known about the elementary conditions needed to create solitons in nematic materials. In this study, we apply a combination of theory, computational simulations, and experiments to examine the formation and propagation of solitary waves, or "solitons", in nematic liquid crystals under the influence of an alternating current (AC) electric field. We find that these solitary waves exhibit "butterfly"-like or "bullet"-like structures that travel in the direction perpendicular to the applied electric field. Such structures propagate over long distances without losing their initial shape. The theoretical framework adopted here helps identify several key factors leading to the formation of solitons in the absence of electrostatic interactions. These factors include surface irregularities, flexoelectric polarization, unequal elastic constants, and negative anisotropic dielectric permittivity. The results of simulations are shown to be in good agreement with our own experimental observations, serving to establish the validity of the theoretical concepts and ideas advanced in this work.**

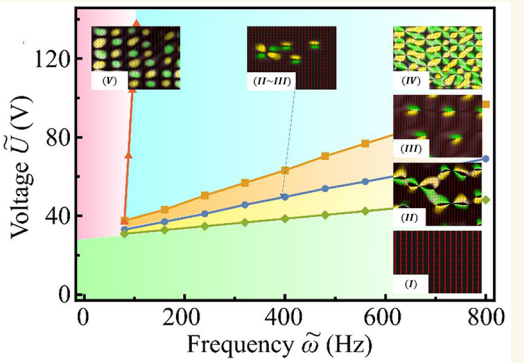

KEYWORDS: *soliton, nematic achiral liquid crystal, flexoelectricity, mechanism of generation, dynamic process*

Solitons are wave packets that maintain their shape while propagating at a constant speed over long distances. This preservation of shape is attributed to a nonlinear feedback mechanism that counteracts dispersion during their journey.[1,2] Solitons have a widespread presence in nature, with manifestations observed in narrow water channels, proteins and DNA, optical fibers, magnets, and even in nuclear physics.[3−6] Several recent reports have documented the emergence of solitons in liquid crystals (LCs) under an applied AC electric field.[7] Potential applications of solitons include long-distance information carriers for optical signals or for particles and chemical species within nematic LCs.

In liquid crystals, three-dimensional solitons are typically observed near surface imperfections, dust particles, or electrode edges, traveling long distnces aperpendicular to the director field.[8,9] Initial observations of such solitons were made by P. Cladis and colleagues[10] decades ago. More recently, several research groups[11−16] have explored solitons from an experimental perspective, while others have considered various underlying theoretical aspects.[17−21]

Recent reports have discussed the motion of topological three-dimensional structures in AC fields, such as twist walls and skyrmions, by invoking the nonreciprocal evolution of the director field.[22−27] These findings illustrate how the "squirming" nonreciprocal evolution of the director, due to the intrinsic properties of nonpolar LCs, can generate the movement of localized solitonic structures. Chirality is believed to play a key role in the formation of these topological structures. Specifically, recent reports indicate that the presence of chirality allows for a broader range of folding modes, and topological solitons with möbiuson structures can be manipulated by adjusting the induced AC field.[28] In our own work, in the process of generating solitons, we find that flexoelectricity plays a central role in the stabilization of solitons, which is reminiscent of the effects of chirality.

Experimental evidence suggests that solitons initially display quadrupolar symmetry at low frequencies, transforming into bullet-like structures with a curved director field at higher

Received: November 1, 2023
Revised: March 15, 2024
Accepted: March 21, 2024
Published: April 10, 2024

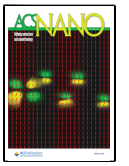

applied fields and frequencies.[11] Bullets can propagate at high speeds, bending along the electric field and exhibiting asymmetry in the solitons' direction of propagation. Most previous experiments indicate that a negative dielectric permittivity anisotropy coupled to an applied alternating electric field is important to generate solitons. A recent study has shown that "frog-egg-like" solitons can be generated in materials with positive anisotropy[15] by adding a relatively high concentration of ions in combination with weak azimuthal anchoring. In this work, we focus on anisotropies of opposite signs, namely, a negative dielectric anisotropy and a positive conductivity anisotropy. Previous studies have posited that the presence of ions and the accumulation of charges due to director irregularities are important factors needed for soliton generation. Experiments have observed that ionic charges accumulate at the surface, leading to a charge modulation that stabilizes the topological defect array.[29] According to Kats' theoretical hypothesis,[20,21] charge injection is believed to be the source of the observed phenomena.

Our simulations reveal several key ingredients necessary for soliton formation in a nematic liquid crystal in the absence of added ions or an inherent chirality. We introduce a minimal model for the tensorial order parameter, which is shown to accurately predict the formation of these solitary waves, in agreement with experimental observations. A negative dielectric permittivity is applied to the liquid crystal to align perpendicularly to the electric field, while flexoelectricity is necessary to stabilize and drive solitons. Surface irregularities are needed to generate director distortions in regions with an inhomogeneous alignment under an applied electric field. Distinct elastic constants are required to penalize different deformation modes as opposed to the commonly used one-constant assumption. We find that these elements are sufficient to generate solitons in the absence of ions. While completely eliminating ions from such systems is challenging, our accompanying experiments are conducted without added salts.[30] We also examine the influence of the electric current of a moving conductor based on Maxwell's equation. Our predictions are compared to experimental data for 4′butyl-4-heptyl-bicyclohexyl-4-carbonitrile (CCN-47).[31,32] Good agreement is found between experiments and simulations.

DISCUSSION

Simulation in DC Field. Before we explore the dynamics of soliton generation and propagation in an AC field, it is essential to first examine the influences of flexoelectricity and surface anomalies under a DC field. For this purpose, we utilize a cubic sample with dimensions of 30 × 20 × 1 and impose Dirichlet boundary conditions at the top and bottom boundaries (at $z = z_{min}$ and $z = z_{max}$, respectively). Periodic boundary conditions are applied along the remaining boundaries in the x and y directions. Initially, the director field is uniform along the x direction. When a DC field aligned along the z-axis is applied, the director field predominantly aligns within the plane orthogonal to the field direction, namely the x−y plane. Our simulations indicate that flexoelectricity and introduced irregularity disrupt the symmetry in the z direction and generate soliton-like structures.

Figure 1 illustrates the director field at the center of the sample (on the x−y plane at $z = 0$ and the x−z plane at $y = 0$), showcasing the influence of flexoelectric effects and surface irregularities. In the depiction, rods represent the three-

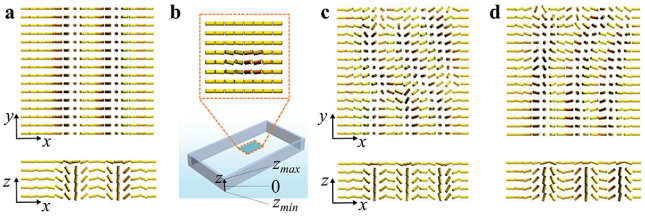

Figure 1. Director field response to a DC field. Panel (a) shows the system relaxing from a uniform initial configuration. Panel (b) depicts a small patch on the top surface introducing a disturbance. Panels (c) and (d) exhibit the director field configurations that develop above the surface patch when the direction of the electric field is alternated. The color intensity of the rods corresponds to the value of s; a lower value of s corresponds to a darker shade.

dimensional nature of the director field. The coloration is light yellow when the director field is parallel to the x−y plane and darkens as it transitions toward the z-axis. Initially, the system is uniform. The application of a static electric field, $\boldsymbol{E} = E_0\hat{\boldsymbol{z}}$, induces splay and bend within the director field due to flexoelectricity, leading to asymmetry along the z-axis in the lower portion of Figure 1a. Figure 1b reveals a localized bullet-like distortion at the center of the surface, disrupting symmetry along the y-axis and forming a periodic pattern that aligns with observations from low-frequency experimental results. Figure 1c and d depict the system from Figure 1b but with the direction of the electric field inverted (with $\boldsymbol{E} = E_0\hat{\boldsymbol{z}}$ and $\boldsymbol{E} = -E_0\hat{\boldsymbol{z}}$, respectively). While both Figure 1a and c exhibit stripe patterns, Figure 1c displays increased distortion due to the applied surface irregularity. The stripe patterns in Figure 1c and d show similarities, yet they are not identical nor mirror images of one another. This is apparent in the differing curvatures along the z-axis. The observed configuration bias is linked to variations in the elastic constants. If the system were modeled under the one-constant assumption, such an asymmetry would be absent, and the patterns would appear as mirrored counterparts. In the Supporting Information, we discuss the transition process from a uniform state.

We applied a step-function electric field, as illustrated in Figure 2a, that oscillates between $\boldsymbol{E} = E_0\hat{\boldsymbol{z}}$ and $\boldsymbol{E} = -E_0\hat{\boldsymbol{z}}$. A

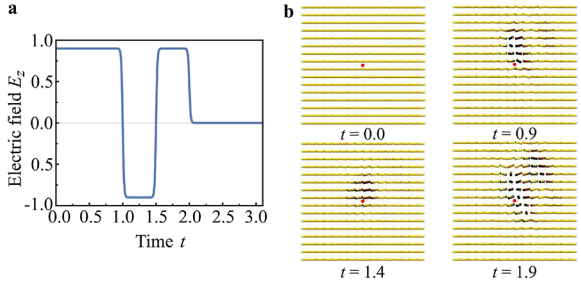

Figure 2. Director field influenced by the reversal of an electric field. Panel (a) shows the simulated system. Panel (b) illustrates the applied electric field. Panel (c) captures the director field on the $z = 0$ plane at various times.

bullet-like distortion, akin to that depicted in Figure 1b, is established at the center of the top surface. Figure 2b shows the director field at the $z = 0$ plane at different times. From $t = 0$ to $t = 1$, the electric field is aligned along the $+z$ axis, causing the director field to be distorted toward the $-z$ axis, and resulting in a butterfly-like structure. Between $t = 1$ and $t = 1.5$,

https://doi.org/10.1021/acsnano.3c10800
ACS Nano 2024, 18, 10768−10775

the electric field shifts to the $-z$ axis, leading to contraction of the director field. As the electric field reverts to the $+z$ axis from $t = 1.5$ to $t = 2$, the director field recovers and expands, showing that the pattern propagates orthogonally to the alignment of both the director and the electric. We switched the direction of the electric field before the director field could relax irreversibly. To clearly trace the pattern, a red dot is placed at the center of the director field.

Simulations reveal that flexoelectricity induces bending and splaying within the director field, disrupting the symmetry about the z-axis. Concurrently, the negative dielectric permittivity facilitates the alignment of the director field along the plane orthogonal to the electric field (the x–y plane). Any irregularity on the surface interrupts the y-axis symmetry, giving rise to a butterfly-like structure near the patch. A reversal in the electric field's direction yields a pattern with a small difference, attributable to the distinct Frank constants. This emerging pattern propels itself in a manner perpendicular to the director field, mirroring the dynamics of solitons observed under an AC field. Investigating the response to a reversed DC field enhances our understanding of soliton genesis.

Simulation in AC Field. In this section, we investigate the behavior of a 3D nematic liquid crystal under a sinusoidal AC field and explore various electric conditions. We generate a phase diagram that resembles those obtained in experimental studies.[30]

For the simulations, we apply a cubic sample with the same dimensions and boundary conditions as described in the previous section. Dirichlet boundary conditions are applied to the top and bottom surfaces ($z = z_{min}$ and $z = z_{max}$), and periodic boundaries are set in the x and y directions. The system's dimensions are $30 \times 20 \times 1$. We introduce a butterfly-like irregularity with homeotropic anchoring on the top surface, while the director field is initially uniform along the x-axis. This butterfly configuration is inspired by earlier research[33] and measures 1×1. A sinusoidal electric field $\boldsymbol{E} = E_0 \sin(\tilde{\omega t})\hat{\boldsymbol{z}}$ is applied, with the electric field strength E_0 ranging from 10 to 100, and frequency $\tilde{\omega}$ changing from 10 to 800. For experimental comparison, we analyze the voltage $\tilde{U} = E_0 d$, where d is the sample thickness. Observations reveal various states emerging at different voltages and frequencies, which are catalogued in a phase diagram (Figure 3). The director field within a plane is delineated using red lines; a uniform director field is indicated in black, while yellow and green represent clockwise and counterclockwise orientations to the z-axis for the director field.[34]

In the phase diagram in Figure 3, Sections I and V are the sections with low voltage and low frequency, respectively. In Section I, the voltage is insufficiently strong to disturb the director field, thus the director field remains almost uniform. Conversely, in Section V, the voltage is adequate to influence the director field, but due to the electric field's long period relative to the material's response time, a periodic pattern emerges. This pattern, known as the R-state,[16] shows similarity to configurations seen under a DC field. Section IV indicates that solitons are rare at high voltages, where the pattern tends to be chaotic.

In Section II, we observe butterfly-like structures. With an increase in the voltage, bullets are emitted along the transition from Section II to Section III. The three-dimensional structure of these bullets is detailed in Figure 3d and elaborated in the Supporting Information. Elevating the voltage further, Section III presents a state characterized by an abundance of bullets and stripes but a reduced presence of butterflies.

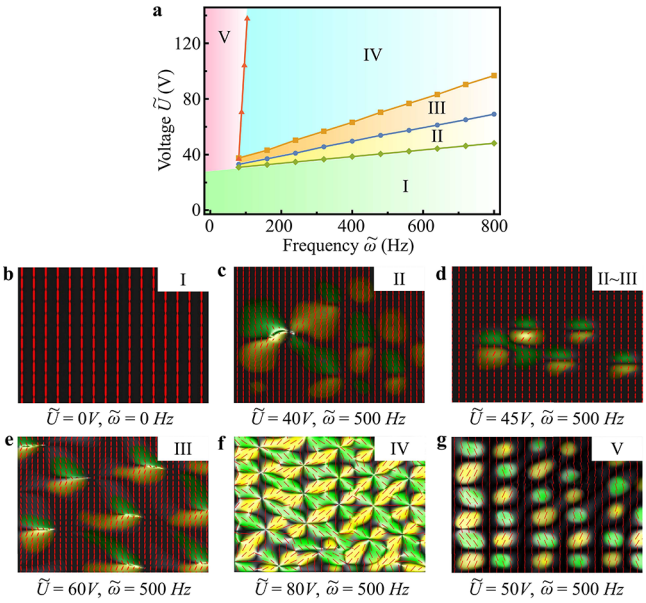

Figure 3. (a) Phase diagram depicting the morphology of a nematic liquid crystal system as influenced by the voltage and frequency under an AC field. Panels (b) to (g) trace the system's transition from a uniform state: (b) illustrates the initial uniform state; (c) shows the emergence of a periodic pattern as voltage increases; (d) captures bullets forming from the butterfly structure; (e) presents a state enriched with bullets; (f) describes the chaotic regime encountered at elevated voltages; and (g) delineates the R-state observed at low frequencies.

Comparison between Simulations and Experiments. In this section, we discuss the process of generating bullets from a localized patch, study the electric conditions for emitting such bullets with different system thicknesses, and compare various states related to the phase diagram presented in the previous section.

It is of interest to examine the contributions of elastic energy F_e, the free energy of dielectric polarization F_{di}, and the flexoelectric polarization (eq 2), as bullets are emitted from the wings of a stable butterfly. We illustrate this process for $\widetilde{E_0} = 42$ and $\tilde{\omega} = 400$ in Figure 4a. These energies are set to zero in the uniform state (the director field is entirely aligned along the x-axis). The elastic energy F_e comprises a combination of splay, bend, and twist contributions. Since the electric field is along the z-axis, the free energy of dielectric polarization F_{di} should increase when more regions of the director field are aligned along the z-axis. From the discussion of the flexoelectric free energy F_{flex} in Section III, it is evident that splay and bend deformations are significant contributors. In Figure 4a, we present the data at the time when $E_z = E_0$, ensuring that F_{flex} is always positive. In the circle and the close-up panel in the figure, we concentrate on the peak of the free energy. The energies are small before $t = 3.4$, where no bullet is emitted from the butterfly. They then increase ($t = 3.4$ to $t = 3.7$) as a new bullet is generated from the upper branch of the butterfly. The peak reaches a maximum ($t = 3.5$) when the bullet is about to be emitted from the butterfly and decreases when the bullet moves away. There are multiple peaks in the figure; each peak represents a newborn bullet emitted from a stationary butterfly.

https://doi.org/10.1021/acsnano.3c10800
ACS Nano 2024, 18, 10768–10775

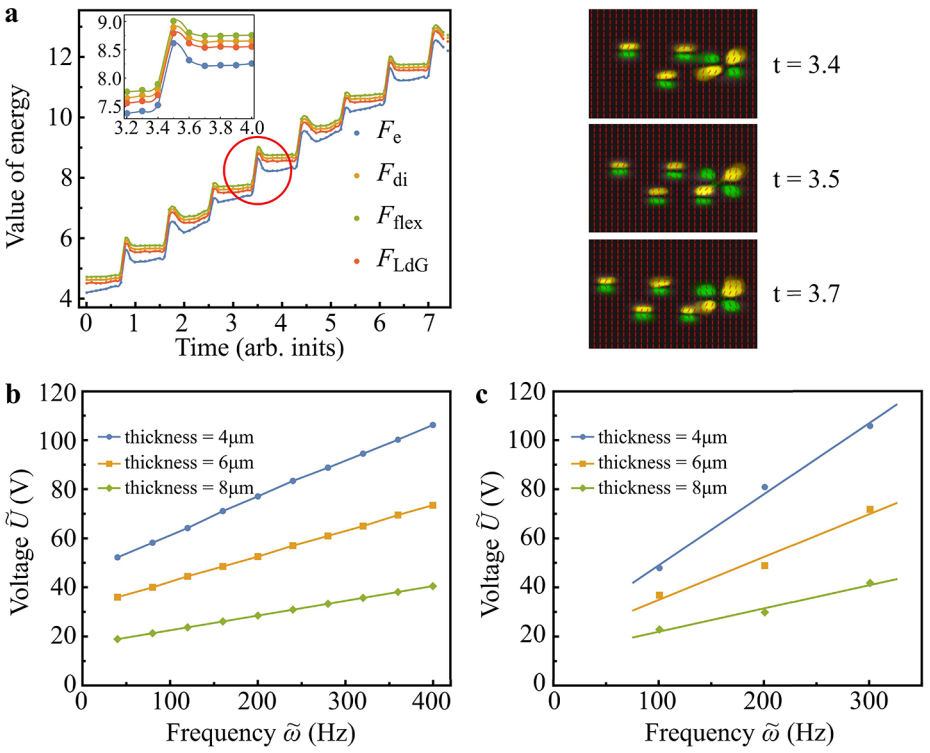

Figure 4. (a) Free energy of the system in the state corresponding to bullets emitted from a stable butterfly (orange band in Figure 3). The inset shows a zoomed-in portion of the free energy corresponding to the emission of an individual bullet. The panels on the right show director field configurations through cross polarizers corresponding to different times in the figure shown in the inset. (b) Results of simulations for the threshold voltage for bullet emission from a butterfly for different sample thicknesses. (c) Experimental results for the threshold voltage for different sample thicknesses.

We also examined the effect of anchoring on soliton formation. Figure 4b and c display the states in which the butterfly structure begins to emit bullets for channels of varying thicknesses. We include results from simulations and experiments. Both sets of results demonstrate that, in a narrower channel where anchoring has a more substantial influence, a higher voltage is required to emit bullets. We find that a linear relationship exists between frequency and voltage. When the voltage is large, the system can rearrange its structure in a short time interval. If the frequency is low, the material has enough time to undergo a complete structural change, and the solitary structure is disrupted. As a result, a higher voltage necessitates a higher frequency if we aim to generate a solitary structure. The inverse relationship between thickness and voltage is observed only within a small range of thicknesses. For greater thicknesses, the effect of confining surfaces diminishes, and solitons are no longer observed, regardless of the applied electric field. This observation is also seen in experiments.[11]

Figure 5 highlights the most relevant regions of the phase diagram, showcasing results from simulations and experiments. When $\tilde{U} = 40$ and $\tilde{\omega} = 400$ (Figure 5a), stable butterflies are observed and remain almost unchanged. When the voltage reaches $\tilde{U} = 45$ at the same frequency (Figure 5c), the butterflies shrink, and the system primarily consists of stripes and bullets. For voltages between these two cases, e.g., $\tilde{U} = 42$ (Figure 5b), we can observe that the bullets emerge from the butterfly created by the surface irregularity. The bullets may originate from any wing of the butterfly and travel over a long distance in a direction perpendicular to the director. When the applied voltage is as high as 45 V, we can observe the chaotic

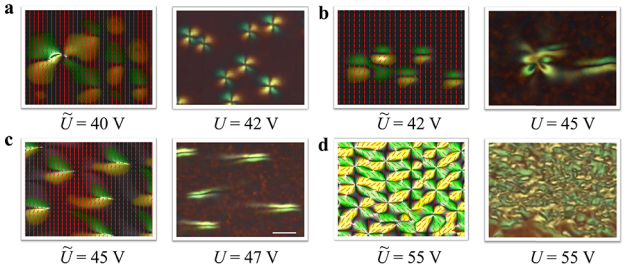

Figure 5. Comparison of results from simulations (left) and experiments (right) corresponding to the director field as observed through cross polarizers for nematic liquid crystals under different applied fields. In (a), several butterflies are observed. In (b), bullets are emitted from the butterfly. In (c), rapidly moving bullets are observed.

regime. In experiments, the same structures are observed for the same frequency but at slightly higher voltages.[30] Note that in liquid crystals, when an electric field is applied, free ions within the material migrate, particularly at the surface or interface of the material, leading to the formation of a double layer structure. Such a double layer could, to some extent, counteract or screen the applied electric field, thereby affecting the distribution and intensity of the electric field within the material.

CONCLUSION

In this work, we investigated the formation and propagation of solitons in a 3D nematic liquid crystal confined between two planar surfaces with planar anchoring. A minimal model of the nematic LC has been used to show that solitons are nucleated

https://doi.org/10.1021/acsnano.3c10800
ACS Nano 2024, 18, 10768−10775

at a surface imperfection with perpendicular anchoring and are generated upon exposure to an AC field. Past reports had suggested that ions are necessary to generate solitons in nematic LCs, and our model and experimental systems indicate that it is also possible to generate solitons without the need to add salts. We find that the key elements are surface inhomogeneity, negative dielectric permittivity, unequal elastic constants, and flexoelectricity. The AC field causes the director field to adopt distinct states periodically, and for sufficiently high frequencies, the material is unable to relax to its stationary structure, thereby emitting solitons that travel at large speeds throughout the system.

The model has been used to construct a state diagram as a function of the strength of the applied field and its frequency. Several regimes are predicted in simulations, including a uniform state, a stripe state, a chaotic state, and a soliton state, which occurs only over a narrow range of voltage strength. Good agreement is obtained between the results of the simulations and our own experimental observations, serving to establish the validity of the model. The findings from this study contribute to foundational knowledge for the development of systems that facilitate the controlled production of solitons. This advances the understanding of soliton applications in areas such as microfluidic transport and technologies related to optics and sensing.

METHODS

We consider a simple 3D thermotropic nematic liquid crystal, where the local orientational order is described by the director field $\hat{\mathbf{n}}(\mathbf{r}, t)$ or the nematic order tensor $Q_{ij}(\mathbf{r}, t)$, and local fluid flow velocity is described by $\mathbf{v}(\mathbf{r}, t)$. To solve the underlying model, we use the method from refs 35 and 36 in three dimensions, which allows the magnitude and direction of the nematic order to vary, so that solitary waves and topological defects can form and move freely.

We quantify the nematic order through a traceless, symmetric tensor:

$$Q_{ij} = s\left(\frac{3}{2}n_i n_j - \frac{1}{2}\delta_{ij}\right) \tag{1}$$

where s is the degree of uniaxial nematic order.

The system's free energy is expressed as follows:

$$\mathcal{F} = \int \mathrm{d}^2 r (f_{\mathrm{LdG}} + f_{\mathrm{elas}} + f_{\mathrm{diel}} + f_{\mathrm{flex}}) \tag{2}$$

In this equation, the free energy density is a sum of four terms: the Landau−de Gennes thermal energy term (f_{LdG}), a contribution of elasticity (f_{elas}), a dielectric energy contribution (f_{diel}), and a term describing the contribution of flexoelectricity (f_{flex}).

The Landau−de Gennes thermal energy term f_{LdG}, also referred to as the enthalpic contribution,[37,38] is expressed as

$$f_{\mathrm{LdG}} = \frac{1}{2}A\mathrm{Tr}(\mathbf{Q})^2 + \frac{1}{3}B\mathrm{Tr}(\mathbf{Q}^3) + \frac{1}{4}C(\mathrm{Tr}(\mathbf{Q}^2))^2 \tag{3}$$

Here, A−C represent thermotropic coefficients. This term describes the nematic to isotropic second-order phase transition with increasing temperature and consists of an expansion of the free energy in powers of Q.

The elastic energy of the nematic phase[39−41] includes all gradient terms of quadratic order in Q allowed by symmetry, plus one term of cubic order,

$$f_{elas} = \frac{L_1}{2}\frac{\partial Q_{ij}}{\partial x_k}\frac{\partial Q_{ij}}{\partial x_k} + \frac{L_2}{2}\frac{\partial Q_{ij}}{\partial x_j}\frac{\partial Q_{ik}}{\partial x_k} + \frac{L_3}{2}\frac{\partial Q_{ik}}{\partial x_j}\frac{\partial Q_{ij}}{\partial x_k} + \frac{L_6}{2}Q_{lk}\frac{\partial Q_{ij}}{\partial x_l}\frac{\partial Q_{ij}}{\partial x_k} \tag{4}$$

where Einstein summation over repeated indices is implied, and L_1 to L_6 are the elastic constants. Here we ignore L_4 and L_5, which describe the saddle-splay and chirality. In this work, we do not make a one-constant approximation, and we estimate the value of L_1 to L_6 based on the Frank constants K_{11}, K_{22}, and K_{33}.

The elastic energy can be described by a combination of splay, twist, and bend in the uniaxial limit (the Frank−Oseen free energy) and can be written as

$$f_{O-F} = \frac{1}{2}K_{11}\boldsymbol{S}^2 + \frac{1}{2}K_{22}\boldsymbol{T}^2 + \frac{1}{2}K_{33}\boldsymbol{B}^2 \tag{5}$$

In this equation, $\boldsymbol{S}$, $\boldsymbol{T}$, and $\boldsymbol{B}$ represent splay, twist, and bend, respectively.[41] Additional details pertaining to the theoretical framework and relationship between L's and K_{ij}'s are provided in the Supporting Information.

The dielectric energy contribution is given by[42,43]

$$f_{\mathrm{diel}} = -\frac{1}{2}\epsilon_0\epsilon_{ij}E_iE_j \tag{6}$$

where ϵ_0 represents the dielectric permittivity of vacuum, and ϵ_{ij} corresponds to the tensorial dielectric permittivity of the nematic material:

$$\epsilon_{ij} = \epsilon_\perp\delta_{ij} + (\epsilon_\parallel - \epsilon_\perp)n_in_j \tag{7}$$

Here, $\epsilon_\perp$ and $\epsilon_\parallel$ are the dielectric permittivities perpendicular and parallel to the nematic field, respectively. By introducing an isotropic dielectric permittivity $\bar{\epsilon} = (2\epsilon_\perp + \epsilon_\parallel)/3$ and a permittivity anisotropy $\epsilon_a = 2(\epsilon_\parallel - \epsilon_\perp)/3s$, one has $\epsilon_{ij} = \bar{\epsilon}\delta_{ij} + \epsilon_aQ_{ij}$.[44,45] The above expressions can be rewritten in terms of the $\mathbf{Q}$-tensor as

$$f_{\mathrm{diel}} = -\frac{1}{2}\epsilon_0(\bar{\epsilon}\delta_{ij} + \epsilon_aQ_{ij})E_iE_j \tag{8}$$

In materials with $\epsilon_a > 0$, the liquid crystal aligns with the electric field. In cases in which ϵ_a is negative, the alignment is transverse. Our model requires a negative dielectric permittivity, which ensures that the director field aligns along the x−y plane (perpendicular to the electric field) rather than along the z-axis (the direction of the electric field). The system is subject to a sinusoidal electric field with frequency ω and maximum electric field E_0 along the z-axis, represented as $\boldsymbol{E} = E_0\sin(\omega t)\hat{\boldsymbol{z}}$.

We can describe the flexoelectricity of the material by adding the term to the electric displacement $\boldsymbol{D}$[46−48]

$$\boldsymbol{P}_f = c_1\partial\cdot\mathbf{Q} + c_2\partial(\mathbf{Q}\cdot\mathbf{Q}) + c_3\partial(\mathrm{Tr}\mathbf{Q}^2) + c_4[\mathbf{Q}\cdot(\partial\mathbf{Q}) - (\mathbf{Q}\cdot\partial)\cdot\mathbf{Q}] \tag{9}$$

The coefficients $c_{1\ldots4}$ are defined in the previous work,[46] and the flexoelectricity term, f_{flex}, can be expressed as

$$f_{\mathrm{flex}} = -\frac{4}{3}\chi_0E_i\partial_jQ_{ij} - \frac{4}{3}\chi_+E_i\partial_j(Q_{ik}Q_{jk}) - \frac{1}{3}\chi_2E_k\partial_k(Q_{ij}Q_{ij}) - \frac{4}{9}\chi_-E_i(Q_{ik}\partial_jQ_{jk} - Q_{jk}\partial_jQ_{ik}) \tag{10}$$

The χ_- term plays a key role in enhancing splay and bend deformations of the director field, thereby amplifying any irregularities caused by surface imperfections, dust particles, or inhomogeneities that contribute to the nucleation of solitary waves. Previous studies have considered the e_{11} and e_{33} terms that represent flexoelectricity,[34,48] where the polarization is given by $\boldsymbol{P} = e_{11}(\hat{\mathbf{n}}\nabla\cdot\hat{\mathbf{n}}) - e_{33}(\nabla\times\hat{\mathbf{n}})\times\hat{\mathbf{n}}$. We introduce an additional term referred to as order polarization.[47] A detailed discussion of this term and our theoretical analysis can be found in the Supporting Information.

Building on previous numerical studies[49−53] and experimental findings,[54,55] we adopt a simplified model that assumes a uniform electric field $\boldsymbol{E}$ and does not integrate Maxwell's equations with the liquid crystal structure in our simulations. However, in the Supporting Information, we outline a methodology to account for the electric field's nonlocality.

https://doi.org/10.1021/acsnano.3c10800
ACS Nano 2024, 18, 10768−10775

To model the temporal evolution of the material, we apply the following equations for dynamic relaxation:

$$\frac{\partial Q_{ij}(\boldsymbol{r}, t)}{\partial t} = -\frac{1}{\gamma_1}\frac{\delta F}{\delta Q_{ij}(\boldsymbol{r}, t)} \tag{11}$$

where γ_1 denotes the rotational viscosity.

We introduce several dimensionless quantities to enable a comparison between our model's predictions and experimental results. In simulations, the characteristic length, denoted by ξ_N, is defined as $\xi_N = \sqrt{CL_1/B^2}$, based on our free energy (2). A characteristic time, τ, is defined as the average time required for a bullet to propagate one unit length and is given by $\Gamma_1\xi^2/L_1$.[56] We solved the differential equations using a finite-element method and the COMSOL software package. The parameters used here are $A = C = 10$, $B = -50$, $L_1 = 5$, $L_2 = 10$, $L_3 = -7.5$, $L_6 = -2.5$, $\chi_0 = -2$, $\chi_+ = 4$, $\chi_2 = -6$, $\chi_- = 5$, $\epsilon_a = -6$, $\bar{\epsilon} = 13$, and $\Gamma_1 = 0.1$. These parameters have been selected based on experimental results through a process of nondimensionalization. The choice of values for A, B, and C is critical. We have found that the system is quite unstable for values between 1 and 10. When these values exceed 100, the order parameter stabilizes at around 1. Specifically, a large value of B results in symmetry breaking, and the existence of a nematic minimum ($s > 0$) is only possible when B is negative and B^2 is greater than $24AC$. With these parameters, the core radius for potential topological defects is the same as the characteristic length, approximately 0.1. Using the following nondimensionalization ratios for voltage and frequency, $\Pi_U = \frac{\chi_-}{L_1}$ and $\Pi_\omega = \tau$, one can determine the real (laboratory) values of the system's state $\tilde{U}$ and $\tilde{\omega}$ (see Supporting Information).

In experiments, the unit of length is set to 50 μm, based on the approximate bullet size of 20 × 50 μm^2. The response time, τ, represents the time required for the nematic to return to equilibrium after the electric field ceases, which is 10^{-2} s; this time is consistent with the period of the AC field in our experiments. At 45 °C, the elastic constants for splay, twist, and bend deformations of CCN-47 are $K_{11} = 6$ pN, $K_{22} = 1$ pN, and $K_{33} = 4$ pN, based on experimental measurements.[30,57,58] The CCN-47 liquid crystal exhibits a large, negative dielectric permittivity of (−5) at 45 °C.[59] The dominant flexoelectricity term, χ_-, is assumed to be 10^{-11} C/m.[11,37]

In the experiment, we prepared surfaces with self-assembled monolayers (SAMs) of alkanethiols on obliquely deposited thin gold films. Gold films were produced by placing glass slides in an electron beam evaporator such that the surface normal of the slides was oriented at a 45° angle relative to the direction of the incoming gold vapor. A thin layer of titanium (20 Å) was first deposited on the glass substrates to promote adhesion of the semitransparent gold layer (200 Å).[60−62] We used a nematic liquid crystal, CCN-47, with negative dielectric permittivity in our experiments. Additional details on the oblique deposition of the gold layer can be found in the Supporting Information.

To prepare surface patches with homeotropic anchoring, we first dispersed 8 μm particles on the gold substrates. This step was followed by immersion in 2 mM ethanolic solutions of 1-hexadecanethiol ($C_{16}SH$). As shown in Figure 6, the presence of the particles ensures that $C_{16}SH$ SAMs are formed everywhere except in locations where the particles block access to the underlying gold. Following the initial round of SAM deposition, the surfaces were thoroughly rinsed with ethanol and water and then sonicated to remove the particles. Next, we immersed the gold substrates in an ethanolic solution of 0.4 mM $C_{16}SH$ + 1.6 mM 1-decanethiol ($C_{12}SH$) to form mixed SAMs in the regions previously occupied by the particles. Our experiments confirm that mixed SAMs formed from the coadsorption of $C_{16}SH$ and $C_{10}SH$ on obliquely deposited thin films of gold are conformationally disordered and give rise to homeotropic or tilted homeotropic LC anchoring of nematic films of CCN-47. The gold surface with this patch of homeotropic anchoring was combined with another gold substrate treated with $C_{16}SH$ (which induces planar anchoring of CCN-47) to form an optical cell as shown in Figure 6. The optical cell was filled with CCN-47 at 70 °C (CCN-47 exhibits a nematic phase between 30.6 and 59.7 °C), followed by cooling to the nematic phase (T = 45 °C). Cross-polar imaging in Figure 6 confirmed the presence of the homeotropic patch on the surface once CCN-47 was introduced into the optical cell. When an electric field (e.g., 260 Hz, 30 V) was applied, the patch preferentially formed a butterfly-like structure, which subsequently emitted a soliton at a higher voltage (260 Hz, 34 V). When the voltage is high, the system goes into a chaotic state even when the frequency is low (80 Hz, 100 V).

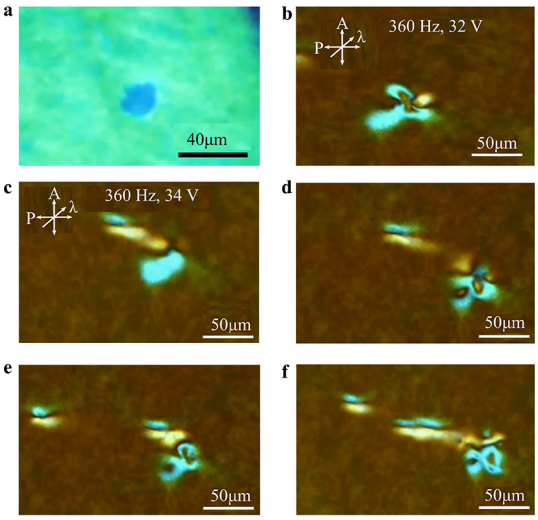

Figure 6. (a) Schematic illustration of the optical cell formed with one surface consisting of a surface patch that promotes homeotropic anchoring of CCN-47. (b) False color image showing the presence of a homeotropic patch when the cell is filled with CCN-47. (c) Cross-polar micrographs depicting the generation of a butterfly-like distortion near the patch in the presence of an electric field. The distortion subsequently emits a soliton (d−f) at a higher applied voltage.

ASSOCIATED CONTENT

Data Availability Statement

The data that support the findings of the study are available from the corresponding author upon reasonable request.

Supporting Information

The Supporting Information is available free of charge at https://pubs.acs.org/doi/10.1021/acsnano.3c10800.

Additional experimental details and analysis, including elastic free energy, flexoelectric free energy, SFG by a gold surface with tilt, numerical details of non-dimensionalization, and 3D structure of soliton. (PDF)

AUTHOR INFORMATION

Corresponding Author

Juan J. de Pablo − *Pritzker School of Molecular Engineering, The University of Chicago, Chicago, Illinois 60637, United States; Center for Molecular Engineering, Argonne National Laboratory, Lemont, Illinois 60439, United States;* orcid.org/0000-0002-3526-516X; Email: depablo@uchicago.edu

Authors

Xingzhou Tang − *Pritzker School of Molecular Engineering, The University of Chicago, Chicago, Illinois 60637, United States; College of Flexible Electronics (Future Technology), Nanjing University of Posts and Telecommunications,*

Nanjing 210023, China; orcid.org/0000-0003-0674-4847

Noe Atzin − *Pritzker School of Molecular Engineering, The University of Chicago, Chicago, Illinois 60637, United States*

Ali Mozaffari − *Pritzker School of Molecular Engineering, The University of Chicago, Chicago, Illinois 60637, United States; OpenEye Scientific, Cadence Molecular Sciences, Boston, Massachusetts 02114, United States*

Soumik Das − *Smith School of Chemical and Biomolecular Engineering, Cornell University, Ithaca, New York 14853, United States; Department of Chemical Engineering, Indian Institute of Technology Kanpur, Kanpur 208016, India;* orcid.org/0000-0002-6997-8280

Nicholas L. Abbott − *Smith School of Chemical and Biomolecular Engineering, Cornell University, Ithaca, New York 14853, United States;* orcid.org/0000-0002-9653-0326

Complete contact information is available at: https://pubs.acs.org/10.1021/acsnano.3c10800

Author Contributions

Xingzhou Tang and Noe Atzin contributed equally to this work. Xingzhou Tang, Noe Atzin, Ali Mozaffari, and Juan de Pablo analyzed the data and discussed the mechanisms. Soumik Das and Nicholas Abbott performed the experimental studies. Juan de Pablo directed the research and the manuscript with inputs from all coauthors.

Notes

The authors declare no competing financial interest.

Statement of the pre-Print Version: This work was submitted to a preprint server as Tang X; Mozaffari A; Atzin N; etc. Generation and propagation of solitary waves in nematic liquid crystals. 2022, arXiv preprint arXiv:2211.01453. https://arxiv.org/abs/2211.01453 (accessed Nov 02, 2022).

ACKNOWLEDGMENTS

This work is supported by the Department of Energy, Basic Energy Sciences, Division of Materials Science and Engineering, Biomaterials Program, under grant no. DESC0019762.

REFERENCES

(1) Dauxois, T.; Peyrard, M. *Physics of solitons*; Cambridge University Press, 2006.

(2) Manton, N.; Sutcliffe, P. *Topological solitons*; Cambridge University Press, 2004.

(3) Heimburg, T.; Jackson, A. D. On soliton propagation in biomembranes and nerves. *Proc. Natl. Acad. Sci. U. S. A.* **2005**, *102*, 9790−9795.

(4) Appali, R.; Van Rienen, U.; Heimburg, T. *Advances in Planar Lipid Bilayers and Liposomes*; Elsevier, 2012; Vol. *16*; pp 275−299.

(5) Andersen, S. S.; Jackson, A. D.; Heimburg, T. Towards a thermodynamic theory of nerve pulse propagation. *Progress in neurobiology* **2009**, *88*, 104−113.

(6) Kartashov, Y. V.; Astrakharchik, G. E.; Malomed, B. A.; Torner, L. Frontiers in multidimensional self-trapping of nonlinear fields and matter. *Nature Reviews Physics* **2019**, *1*, 185−197.

(7) Lam, L. *Solitons in Liquid Crystals*; Springer, 1992; pp 9−50.

(8) Das, S.; Atzin, N.; Tang, X.; Mozaffari, A.; de Pablo, J.; Abbott, N. L. Jetting and Droplet Formation Driven by Interfacial Electrohydrodynamic Effects Mediated by Solitons in Liquid Crystals. *Phys. Rev. Lett.* **2023**, *131*, 098101.

(9) Atzin, N.; Mozaffari, A.; Tang, X.; Das, S.; Abbott, N. L.; de Pablo, J. J. Minimal Model of Solitons in Nematic Liquid Crystals. *Phys. Rev. Lett.* **2023**, *131*, 188101.

(10) Brand, H. R.; Fradin, C.; Finn, P.; Pesch, W.; Cladis, P. Electroconvection in nematic liquid crystals: comparison between experimental results and the hydrodynamic model. *Phys. Lett. A* **1997**, *235*, 508−514.

(11) Li, B.-X.; Borshch, V.; Xiao, R.-L.; Paladugu, S.; Turiv, T.; Shiyanovskii, S. V.; Lavrentovich, O. D. Electrically driven three-dimensional solitary waves as director bullets in nematic liquid crystals. *Nat. Commun.* **2018**, *9*, 1−10.

(12) Shen, Y.; Dierking, I. Recent progresses on experimental investigations of topological and dissipative solitons in liquid crystals. *Crystals* **2022**, *12*, 94.

(13) Shen, Y.; Dierking, I. Dynamics of electrically driven solitons in nematic and cholesteric liquid crystals. *Communications physics* **2020**, *3*, 14.

(14) Shen, Y.; Dierking, I. Electrically driven formation and dynamics of swallow-tail solitons in smectic A liquid crystals. *Materials Advances* **2021**, *2*, 4752−4761.

(15) Shen, Y.; Dierking, I. Dynamic dissipative solitons in nematics with positive anisotropies. *Soft Matter* **2020**, *16*, 5325−5333.

(16) Aya, S.; Araoka, F. Kinetics of motile solitons in nematic liquid crystals. *Nat. Commun.* **2020**, *11*, 1−10.

(17) Cladis, P.; Brand, H. R. Hedgehog−antihedgehog pair annihilation to a static soliton. *Physica A: Statistical Mechanics and its Applications* **2003**, *326*, 322−332.

(18) Pesch, W.; Krekhov, A.; Éber, N.; Buka, Á. Nonlinear analysis of flexodomains in nematic liquid crystals. *Phys. Rev. E* **2018**, *98*, 032702.

(19) Chuvyrov, A.; Krekhov, A.; Lebedev, Y. A.; Timirov, Y. I. Soliton-like defects in nematic liquid crystal thin layers. *Journal of Experimental and Theoretical Physics* **2016**, *123*, 899−907.

(20) Dolganov, P. V.; Zhilin, V. M.; Dolganov, V. K.; Kats, E. I. Formation and structure of a soliton in an antiferroelectric liquid crystal in an electric field. *JETP letters* **2009**, *89*, 161−166.

(21) Pikina, E.; Kats, E.; Muratov, A.; Lebedev, V. *Nonlinear electrohydrodynamics of liquid crystals. arXiv preprint arXiv:2210.09613* **2022**.

(22) Long, C.; Selinger, J. V. Coarse-grained theory for motion of solitons and skyrmions in liquid crystals. *Soft Matter* **2021**, *17*, 10437−10446.

(23) Ackerman, P. J.; Boyle, T.; Smalyukh, I. I. Squirming motion of baby skyrmions in nematic fluids. *Nat. Commun.* **2017**, *8*, 673.

(24) Duzgun, A.; Nisoli, C.; Reichhardt, C.; Reichhardt, C. Directed motion of liquid crystal skyrmions with oscillating fields. *New J. Phys.* **2022**, *24*, 033033.

(25) Sohn, H. R.; Liu, C. D.; Smalyukh, I. I. Schools of skyrmions with electrically tunable elastic interactions. *Nat. Commun.* **2019**, *10*, 4744.

(26) Panov, V. P.; Yang, J.; Migara, L.; Yoon, H.-J.; Song, J.-K. Rotation-Time Symmetry Breaking in Frustrated Chiral Nematic Driven by a Pulse-Train Waveform. *Phys. Rev. Lett.* **2022**, *129*, 117801.

(27) Alvim, T.; da Gama, M. M. T.; Tasinkevych, M. *Coarse grained model for skyrmion dynamics. arXiv preprint arXiv:2304.12884* **2023**.

(28) Zhao, H.; Tai, J.-S. B.; Wu, J.-S.; Smalyukh, I. I. Liquid crystal defect structures with Möbius strip topology. *Nat. Phys.* **2023**, *19*, 451−459.

(29) Sasaki, Y.; Jampani, V.; Tanaka, C.; Sakurai, N.; Sakane, S.; Le, K. V.; Araoka, F.; Orihara, H. Large-scale self-organization of reconfigurable topological defect networks in nematic liquid crystals. *Nat. Commun.* **2016**, *7*, 13238.

(30) Das, S.; Roh, S.; Atzin, N.; Mozaffari, A.; Tang, X.; de Pablo, J. J.; Abbott, N. L. Programming Solitons in Liquid Crystals Using Surface Chemistry. *Langmuir* **2022**, *38*, 3575−3584.

(31) Zawadzki, A.; Walton, H. Measurements of the splay and bend elastic constants of 4′-butyl-4-heptyl-bicyclohexyl-4-carbononitrile, CCN47. *Mol. Cryst. Liq. Cryst.* **2012**, *569*, 10−14.

(32) Lucchetti, L.; Nava, G.; Barboza, R.; Ciciulla, F.; Bellini, T. Optical force-based detection of splay and twist viscoelasticity of CCN47 across the Nematic-to-Smectic A transition. *J. Mol. Liq.* **2021**, *329*, 115520.

(33) Earls, A.; Calderer, M. C. Three-dimensional soliton-like distortions in flexoelectric nematic liquid crystals: modelling and linear analysis. *Liq. Cryst.* **2022**, *49*, 742−757.
(34) Lavrentovich, O. D. Design of nematic liquid crystals to control microscale dynamics. *Liquid Crystals Reviews* **2020**, *8*, 59−129.
(35) Tang, X.; Selinger, J. V. Orientation of topological defects in 2D nematic liquid crystals. *Soft Matter* **2017**, *13*, 5481−5490.
(36) Tang, X.; Selinger, J. V. Theory of defect motion in 2D passive and active nematic liquid crystals. *Soft Matter* **2019**, *15*, 587−601.
(37) De Gennes, P.-G.; Prost, J. *The physics of liquid crystals*; Oxford University Press, 1993.
(38) Grebel, H.; Hornreich, R.; Shtrikman, S. Landau theory of cholesteric blue phases. *Phys. Rev. A* **1983**, *28*, 1114.
(39) Mori, H.; Gartland, E. C.; Kelly, J. R.; Bos, P. J. Multidimensional director modeling using the Q tensor representation in a liquid crystal cell and its application to the it cell with patterned electrodes. *Japanese Journal of Applied Physics, Part 1: Regular Papers and Short Notes and Review Papers* **1999**, *38*, 135−146.
(40) Nehring, J.; Saupe, A. Calculation of the Elastic Constants of Nematic Liquid Crystals. *J. Chem. Phys.* **1972**, *56*, 5527−5528.
(41) Selinger, J. V. Interpretation of saddle-splay and the Oseen-Frank free energy in liquid crystals. *Liquid Crystals Reviews* **2018**, *6*, 129−142.
(42) Landau, L. D.; Lifshitz, E. M. *Fluid Mechanics: Landau and Lifshitz: Course of Theoretical Physics, Vol. 6*; Elsevier Science, 2013.
(43) Porenta, T.; Ravnik, M.; Zumer, S. Effect of flexoelectricity and order electricity on defect cores in nematic droplets. *Soft Matter* **2011**, *7*, 132−136.
(44) Parry-Jones, L. A.; Meyer, R. B.; Elston, S. J. Mechanisms of flexoelectric switching in a zenithally bistable nematic device. *J. Appl. Phys.* **2009**, *106*, 14510.
(45) Palto, S. P.; Mottram, N. J.; Osipov, M. A. Flexoelectric instability and a spontaneous chiral-symmetry breaking in a nematic liquid crystal cell with asymmetric boundary conditions. *Phys. Rev. E* **2007**, *75*, 061707.
(46) Blow, M. L.; da Gama, M. T. Interfacial motion in flexo-and order-electric switching between nematic filled states. *J. Phys.: Condens. Matter* **2013**, *25*, 245103.
(47) Barbero, G.; Dozov, I.; Palierne, J.; Durand, G. Order electricity and surface orientation in nematic liquid crystals. *Physical review letters* **1986**, *56*, 2056.
(48) Alexe-Ionescu, A.-L. Flexoelectric polarization and second order elasticity for nematic liquid crystals. *Phys. Lett. A* **1993**, *180*, 456−460.
(49) Davidson, A.; Brown, C.; Mottram, N.; Ladak, S.; Evans, C. Defect trajectories and domain-wall loop dynamics during two-frequency switching in a bistable azimuthal nematic device. *Phys. Rev. E* **2010**, *81*, 051712.
(50) Denniston, C.; Yeomans, J. Flexoelectric surface switching of bistable nematic devices. *Physical review letters* **2001**, *87*, 275505.
(51) Davidson, A.; Mottram, N. Flexoelectric switching in a bistable nematic device. *Phys. Rev. E* **2002**, *65*, 051710.
(52) Sulaiman, N.; Marenduzzo, D.; Yeomans, J. Lattice Boltzmann algorithm to simulate isotropic-nematic emulsions. *Phys. Rev. E* **2006**, *74*, 041708.
(53) Alexander, G.; Yeomans, J. Flexoelectric blue phases. *Physical review letters* **2007**, *99*, 067801.
(54) Ryzhkova, A.; Podgornov, F.; Haase, W. Nonlinear electrophoretic motion of dielectric microparticles in nematic liquid crystals. *Appl. Phys. Lett.* **2010**, *96*. DOI: 10.1063/1.3386570
(55) Lavrentovich, O. D.; Lazo, I.; Pishnyak, O. P. Nonlinear electrophoresis of dielectric and metal spheres in a nematic liquid crystal. *Nature* **2010**, *467*, 947−950.
(56) Armas-Pérez, J. C.; Hernández-Ortiz, J. P.; de Pablo, J. J. Liquid crystal free energy relaxation by a theoretically informed Monte Carlo method using a finite element quadrature approach. *J. Chem. Phys.* **2015**, *143*, 243157.
(57) Lucchetti, L.; Nava, G.; Barboza, R.; Ciciulla, F.; Bellini, T. Optical force-based detection of splay and twist viscoelasticity of CCN47 across the Nematic-to-Smectic A transition. *J. Mol. Liq.* **2021**, *329*, 115520.
(58) Sai, D. V.; Zuhail, K.; Sarkar, R.; Dhara, S. Structure−property correlation of bicyclohexane nematic liquid crystals. *Liq. Cryst.* **2015**, *42*, 328−333.
(59) Dhara, S.; Madhusudana, N. Physical characterisation of 4′butyl-4-heptyl-bicyclohexyl-4-carbonitrile. *Phase Transitions* **2008**, *81*, 561−569.
(60) Gupta, V. K.; Abbott, N. L. Uniform anchoring of nematic liquid crystals on self-assembled monolayers formed from alkanethiols on obliquely deposited films of gold. *Langmuir* **1996**, *12*, 2587−2593.
(61) Skaife, J. J.; Abbott, N. L. Quantitative characterization of obliquely deposited substrates of gold by atomic force microscopy: influence of substrate topography on anchoring of liquid crystals. *Chemistry of materials* **1999**, *11*, 612−623.
(62) Follonier, S.; Miller, W.; Abbott, N.; Knoesen, A. Characterization of the Molecular Orientation of Self-Assembled Monolayers of Alkanethiols on Obliquely Deposited Gold Films by Using Infrared-Visible Sum-Frequency Spectroscopy. *Langmuir* **2003**, *19*, 10501−10509.

https://doi.org/10.1021/acsnano.3c10800
ACS Nano 2024, 18, 10768−10775